Editors' Suggestion

Scalable Quantum Logic Spectroscopy

Kaifeng Cui,[1,2,3,*] Jose Valencia,[1,4] Kevin T. Boyce,[1,4] Ethan R. Clements,[1,4] David R. Leibrandt,[1,4] and David B. Hume[1,†]

[1]National Institute of Standards and Technology, Boulder, Colorado 80305, USA
[2]HEP Division, Argonne National Laboratory, Lemont, Illinois 60439, USA
[3]Key Laboratory of Atomic Frequency Standards, Innovation Academy for Precision Measurement Science and Technology, Chinese Academy of Sciences, Wuhan 430071, China
[4]Department of Physics, University of Colorado, Boulder, Colorado 80305, USA

(Received 17 April 2022; revised 24 July 2022; accepted 30 September 2022; published 2 November 2022)

In quantum logic spectroscopy (QLS), one species of trapped ion is used as a sensor to detect the state of an otherwise inaccessible ion species. This extends precision measurements to a broader class of atomic and molecular systems for applications like atomic clocks and tests of fundamental physics. Here, we develop a new technique based on a Schrödinger cat interferometer to address the problem of scaling QLS to larger ion numbers. We demonstrate the basic features of this method using various combinations of $^{25}Mg^+$ logic ions and $^{27}Al^+$ spectroscopy ions. We observe higher detection efficiency by increasing the number of $^{25}Mg^+$ ions. Applied to multiple $^{27}Al^+$, this method will improve the stability of high-accuracy optical clocks and could enable Heisenberg-limited QLS.

DOI: 10.1103/PhysRevLett.129.193603

Experiments on quantum systems face a common challenge of state detection, which requires amplifying tiny quantum signals above the background noise. In the case of atomic systems, including trapped ions, the typical approach to state detection is to observe photons scattered from a particular quantum state [1]. This approach works well on a limited number of atomic species that have a suitable internal structure; however, numerous other atomic species are compelling targets for specific applications but do not have suitable transitions for direct state detection. For example, some species of molecular ions [2,3], highly charged ions [4], and even antimatter particles [5] offer unique opportunities for testing fundamental physics [6].

Quantum logic spectroscopy (QLS) enables state detection of otherwise inaccessible ions by introducing a cotrapped logic ion (LI). The internal state of the spectroscopy ion (SI) is transferred via a shared mode of motion to the LI where it can be detected via photon scattering. The first demonstration of QLS was with $^{27}Al^+$ [7,8], which now serves as a frequency reference in atomic clocks [9–12]. Variations on the QLS technique have been developed with several aims: to demonstrate Hz-level precision spectroscopy for atomic clocks [9–12], to perform correlation spectroscopy [13], to work far off resonance from an optical transition [2,14], or to operate in thermal motion [15,16]. So far, QLS has only been performed on up to two SIs [13] and the issue of scaling QLS techniques to larger ion numbers [17] is an open experimental question.

In this Letter, we propose and experimentally demonstrate a new method of QLS that can be scaled to larger ion numbers. Our protocol employs multiple LIs as independent sensors to detect a state-dependent driving force applied to the cotrapped SIs. This technique does not require ground-state cooling or individual ion addressing, both of which become more difficult with larger ion ensembles [18,19]. We apply the technique experimentally to ensembles of up to three LIs and three SIs. By scaling the number of LIs, we show that technical noise in the detection process can be suppressed.

Our protocol relies on a Schrödinger cat state [20] of the LIs, which acts as an interferometric sensor for the state of the SIs (see Fig. 1). Several schemes have been explored to create the Schrödinger cat states [20–23], including the $\hat{\sigma}_\phi$-type interaction [22,24] employed here. To produce this, a bichromatic laser field is applied to the LIs with frequency components near resonance with the motional sidebands at frequencies $\omega_0 \pm \omega_M$, where ω_0 is the qubit resonance frequency and ω_M is the frequency of a shared motional mode. In the Lamb-Dicke limit, the dynamics of a single LI driven by the laser are described by the interaction Hamiltonian [25],

$$\hat{H} = \frac{\hbar\eta\Omega_0}{2}\hat{\sigma}_\phi(\hat{a}e^{i\phi_M} + \hat{a}^\dagger e^{-i\phi_M}), \tag{1}$$

where $2\pi\hbar$ is Planck's constant, Ω_0 is the Rabi frequency, and η is the Lamb-Dicke parameter, describing the coupling strength between the laser field and the motional mode of the ions. We use a rotated Pauli spin operator $\hat{\sigma}_\phi = e^{-i\phi_S}\hat{\sigma}_+ + e^{i\phi_S}\hat{\sigma}_-$, where $\hat{\sigma}_\pm$, $\hat{a}$, and $\hat{a}^\dagger$ are ladder operators of the spin mode and the motional mode, respectively. The phases of the red (ϕ_r) and blue (ϕ_b)

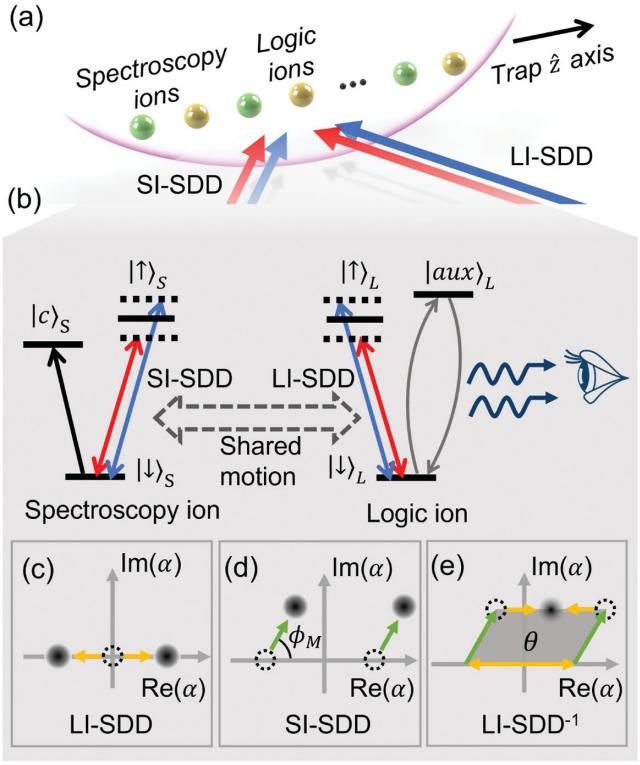

FIG. 1. (a) An ensemble of SIs (green dots) and LIs (yellow dots) confined within a linear ion trap. The arrows indicate SDDs provided by two bichromatic laser fields. (b) The energy levels involved in these experiments. (c)–(e) Schrödinger cat interferometry sequence in motional phase space.

components of the laser field control the spin phase $\phi_S = (\phi_b + \phi_r)/2$ and the motional phase $\phi_M = (\phi_b - \phi_r)/2$.

In the simplest case, consider a single LI prepared in a superposition state: $|\psi\rangle_L = |\downarrow\rangle_L = (|\rightarrow\rangle_L + |\leftarrow\rangle_L)/\sqrt{2}$, where $|\uparrow\rangle_L$ and $|\downarrow\rangle_L$ are the energy eigenstates of the LI and $|\leftarrow\rangle_L$ and $|\rightarrow\rangle_L$ are the eigenstates of $\hat{\sigma}_\phi$. Applying the bichromatic laser field realizes a spin-dependent displacement on the LI (LI-SDD): $\hat{\mathcal{U}}(t) = \hat{\mathcal{D}}(+\alpha)|\rightarrow\rangle_L\langle\rightarrow|_L + \hat{\mathcal{D}}(-\alpha)|\leftarrow\rangle_L\langle\leftarrow|_L$, where $\mathcal{D}$ is the motional phase space displacement amplitude and $\alpha(t) = -i\eta\Omega_0 t e^{-i\phi_M}/2$. This is analogous to the first "beam splitter" of an interferometer, creating the Schrödinger cat state shown in Fig. 1(c). Likewise, the second beam splitter in the interferometer (LI-SDD^{-1}) can be produced by applying the same laser pulse, but shifting ϕ_M by π. If there is no additional displacement during the interferometer, this operation recombines the two motional components, recovering the initial state of the LI. However, displacements that occur between the two interferometer pulses generally produce a geometric phase, which can be detected in the final state of the LI. Here, we consider a state-dependent displacement (SI-SDD) produced by another bichromatic laser field applied to a SI coupled to the LI through their collective motion at frequency ω_M. For example, if the SI is prepared

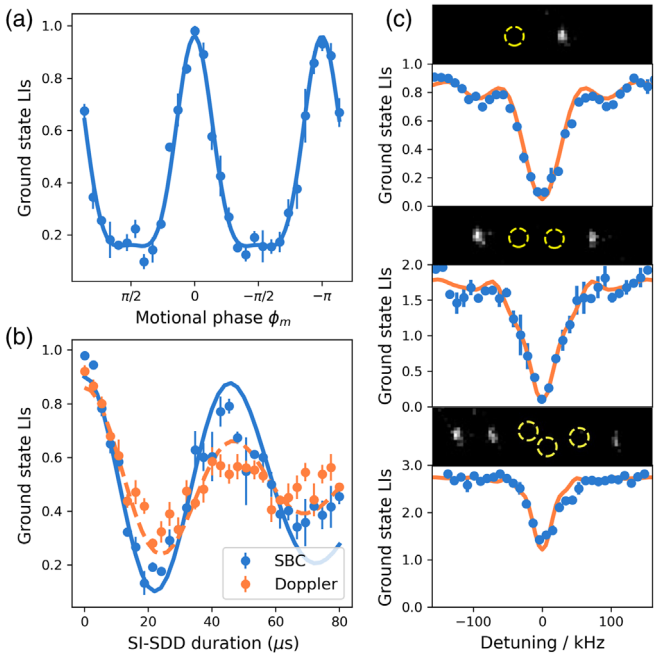

FIG. 2. Quantum logic spectroscopy using a Schrödinger cat interferometer. (a) Using one $^{25}Mg^+$ as a LI and one $^{27}Al^+$ ion as a SI, the ground-state probability of the LI ($P_{\downarrow,L}$) is modulated by the geometric phase encoded in phase space when scanning the motional phase angle ϕ_M. Experimental results (blue points) match the fit of Eq. (2) (solid line). (b) The duration of LI-SDD is scanned with ions cooled to the Doppler limit (orange points) and after sideband cooling (blue points). Lines are the results of numerical simulations without free parameters. (c) Spectroscopy of the $^1S_0 \rightarrow {}^3P_1$ transition of one, two, and three $^{27}Al^+$ SIs using equal number of $^{25}Mg^+$ LIs. Insets on the top of each figure are fluorescence images of the $^{25}Mg^+$ ions (bright spots). $^{27}Al^+$ ion positions are marked in yellow circles based on theoretical calculations. The data (blue circles) are fit by numerical simulations (orange line). Error bars represent one standard deviation of the LI quantum projection noise. Note that, for the case of six ions, the ion chain has formed a zigzag geometry, but we still observe a resonant response in the interferometer, although with reduced contrast.

in the state $|\psi\rangle_S = (|\downarrow\rangle_S + |\uparrow\rangle_S)/\sqrt{2} = |\rightarrow\rangle_S$, it undergoes a displacement $\hat{\mathcal{D}}(\beta)$ [marked as SI-SDD in Fig. 1(d)], which produces a geometric phase $\theta = 2\alpha\beta\sin\phi_M$, rotating the state of the LI by $e^{-2i\theta\hat{\sigma}_\phi}$. Measurement of the LI population $P_{\downarrow,L}$ after the second beam splitter gives

$$P_{\downarrow,L} = [1 + \cos(4\alpha\beta\sin\phi_M)]/2. \quad (2)$$

The parameter β contains information about the interaction between the SI and the SI-SDD beams, which is detected interferometrically by the LI. We use this in two distinct ways. First, we perform spectroscopy directly on the $|\downarrow\rangle_S \leftrightarrow |\uparrow\rangle_S$ transition, where the phase, duration, and detuning of the SI-SDD pulse itself modulates β (Fig. 2).

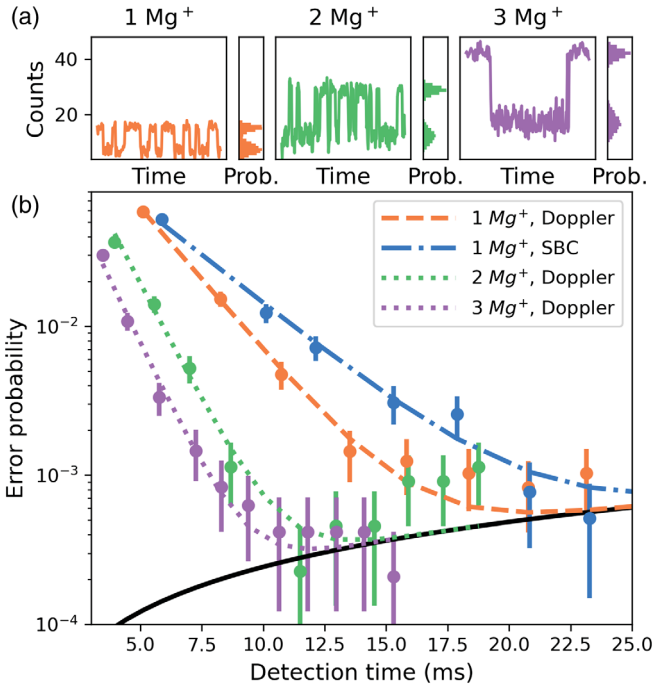

FIG. 3. Scaling the number of LIs to improve the detection efficiency of a single SI. (a) Transitions between $|\downarrow\rangle_S$ and $|c\rangle_S$ control the output of the interferometer resulting in quantum jumps in the fluorescence of the LIs. Each of the data points is an average of 20 measurements, where a single measurement takes 1.8 ms. The histograms on the right show the full distribution of these data (1500 data points; Prob, probability density). (b) Observed error rate estimate comes from the comparison of two consecutive detection sequences during the detection. Error bars are symmetric, based on the standard variance of a Poisson distribution. The black solid line represents the lifetime-limited error probability due to the spontaneous decay of the $|c\rangle_S$ state.

Second, we detect "clock" transitions from $|\downarrow\rangle_S$ to the long-lived clock state ($|c\rangle_S$) using the fact that only the ions in state $|\downarrow\rangle_S$ interact with the SI-SDD pulse. This allows for spectroscopy on a narrow clock transition and is analogous to the electron-shelving technique used in conventional fluorescence measurements (Fig. 3).

Both protocols can be scaled to N_L LIs and N_S SIs. Assuming that all ions have nearly equal mode amplitudes and feel equal driving forces, all the LIs can be treated as independent sensors. The signal observed by the LIs increases linearly with N_L [26]. In scaling N_S, the force experienced by the ions during the SI-SDD pulse increases linearly with the number of SIs in the state $|\downarrow\rangle_S$. By appropriate choice of parameters α and ϕ_M this provides a means to count the number of ions remaining in $|\downarrow\rangle_S$ after a clock pulse on multiple SIs.

We demonstrate this interferometer using $^{25}Mg^+$ as the LI and $^{27}Al^+$ as the SI confined in a linear Paul trap [12,27]. The trap frequencies are approximately $(\omega_x, \omega_y, \omega_z) = 2\pi \times (6.7, 6.3, 2.5)$ MHz for a single $^{25}Mg^+$. The qubit states of the $^{25}Mg^+$ ions are encoded in $|\downarrow\rangle_L \equiv |^2S_{1/2}, F = 3, m_F = -3\rangle$ and $|\uparrow\rangle_L \equiv |^2S_{1/2}, F = 2, m_F = -2\rangle$. Doppler cooling and state detection of $^{25}Mg^+$ relies on resonance fluorescence from the $|\downarrow\rangle_L \leftrightarrow |^2P_{3/2}, F = 4, m_F = -4\rangle$ cycling transition driven by a circularly polarized 280.4 nm laser beam.

A pair of perpendicular 279.6 nm laser beams, referred to here as red Raman and blue Raman (BR), respectively, with wave vector difference $\Delta\boldsymbol{k}$ along the trap z axis are used to generate Raman sideband pulses [27] and the LI-SDD. The BR beam consists of two frequency components, which are separated by $2\omega_M$. For the $^{27}Al^+$ ions, the qubit states are encoded in $|\downarrow\rangle_S \equiv |^1S_0, m_F = -5/2\rangle$ and $|\uparrow\rangle_S \equiv |^3P_1, m_F = -7/2\rangle$. A circular-polarized, bichromatic 266.9 nm beam line is applied at a 45° angle with the trap z axis for the qubit manipulation and the SI-SDD. Both the 266.9 and 279.6 nm laser beams are intensity stabilized using photodiodes before entering the trap to generate carrier Rabi rates of approximately 300 kHz. When trapping one $^{25}Mg^+$ ion and one $^{27}Al^+$ ion, the Lamb-Dicke parameters of the 2.5 MHz c.m. mode along the z axis are $\eta_L = 0.18$ for the LI and $\eta_S = 0.10$ for the SI, respectively. We use this mode to drive both the LI-SDD and the SI-SDD, as the mode amplitudes z_0 are nearly the same for ions in different positions. In addition, the motional phases of both SDDs need to be equal for all the ions and controllable between species, which can be satisfied using a bichromatic laser field [26]. When scaling to a multiple number of ions, those Lamb-Dicke parameters decrease since the ground-state wave function size $z_0 \propto (M\omega_M)^{-1/2}$, where M is the total mass of the ion chain.

We first prepare a pair of $^{25}Mg^+$ and $^{27}Al^+$ to demonstrate features of the interferometer. The $^{25}Mg^+$ ion is optically pumped to the $|\downarrow\rangle_L$ state, while the $^{27}Al^+$ ion is rotated to $|\rightarrow\rangle_S = (|\downarrow\rangle_S + |\uparrow\rangle_S)/2$ using a $\pi/2$ carrier pulse. In order to control the geometric phase enclosed in the interferometer, it is necessary to maintain the relative phases between the LI-SDD on the $^{25}Mg^+$ ions and SI-SDD on the $^{27}Al^+$ ions. To accomplish this, we produce the red and blue tones for the two bichromatic laser beams by mixing radio-frequency signals that are used to drive two acousto-optic modulators from a single source [26]. The long-term phase coherence can be observed between these two pairs of laser beams by scanning their relative phase ϕ_M [Fig. 2(a)]. In this experiment, we have calibrated $4\alpha\beta = \pi$ and the solid line is a fit based on Eq. (3). In the following experiments, we set $\phi_M = \pi/2$ to maximize the geometric phase.

By scanning the duration of the SI-SDD (Fig. 2) we observe how the detection signal varies as a function of β. We include experimental results when the ions are cooled close to the Doppler limit and with 1.25 ms of additional sideband cooling (SBC). Both cases are affected by higher-order terms in the Hamiltonian beyond the Lamb-Dicke limit, which appears as a loss in contrast of the detection signal as a function of the SI-SDD pulse time. Because of

higher temperature, this effect is more significant for the Doppler-cooled case.

We use this interferometer to perform spectroscopy of the $^1S_0 \rightarrow {}^3P_1$ transition of up to three $^{27}Al^+$ ions cotrapped with the same number of $^{25}Mg^+$ ions. The duration of both LI-SDD and SI-SDD pulses are calibrated on resonance to make the geometric phase enclosed within the interferometer $2N_S\alpha\beta = \pi/2$. The detuning between the 266.9 nm laser beam and the $^1S_0 \rightarrow {}^3P_1$ transition (δ_s) is scanned over a range of 300 kHz. Additional SBC pulses are applied for all the cases to suppress the coupling outside the Lamb-Dicke regime. We note that when $\delta_s \neq 0$, the $^{27}Al^+$ ions and the collective motion undergo a complicated evolution, resulting in a complex line shape shown in the simulation results (see Supplemental Material [26]).

Now we introduce the SI clock state ($|c\rangle_S$) encoded in the $|^3P_0, m_F = -5/2\rangle$ state which has a lifetime of approximately 20.6 s [28]. Precision measurement of the $|\downarrow\rangle_S \leftrightarrow |c\rangle_S$ transition is the basis for Al^+ optical clocks. We use a single $^{27}Al^+$ ion and vary the number of $^{25}Mg^+$ ions from 1 to 3. The $^{27}Al^+$ ion is driven periodically by a weak 267.4 nm laser that is close to resonance with the clock transition resulting in infrequent state changes. These "quantum jumps" are clearly observed [Fig. 3(a)] since the SI-SDD, and hence the fluorescence of the $^{25}Mg^+$ ions is gated by the state of the $^{27}Al^+$ ion.

We select the number of measurement repetitions via an adaptive Bayesian process [8]. The detection error probability is determined by comparing the results of two consecutive detection sequences [Fig. 3(b)], counting one detection error if they disagree. This assumes that the probability of two consecutive detection errors can be ignored, which is true for small, uncorrelated error probabilities. We expect this to be valid for shorter detection times [the initial slopes in Fig. 3(b)], but errors due to spontaneous decay at longer detection times will violate the assumption of uncorrelated errors [29]. We observe that increasing the number of $^{25}Mg^+$ ions increases the measurement efficiency. In addition to the improved signal-to-noise ratio, given the same confinement conditions, the Lamb-Dicke parameters are also reduced with more LIs, improving the contrast by suppressing imperfections due to higher-order processes.

In Fig. 3(b), we also compare the efficiency of detection at the Doppler limit versus after sideband cooling the z c.m. mode to near the motional ground state. Although the single-shot fidelity is lower with only Doppler cooling, the 1.25 ms additional duration of the sideband cooling sequence makes it less efficient.

We demonstrate the detection protocol with two $^{27}Al^+$ and two $^{25}Mg^+$ ions ($N_S = N_L = 2$). We introduce the number states $|N_{S,\downarrow}\rangle$ to represent the number of SIs remaining in state $|\downarrow\rangle_S$, where $|N_{S,\downarrow}\rangle \in \{|0\rangle, |1\rangle, |2\rangle\}$. In Fig. 4(a), we show expected fluorescence levels for each of these three cases as a function of the SI-SDD duration.

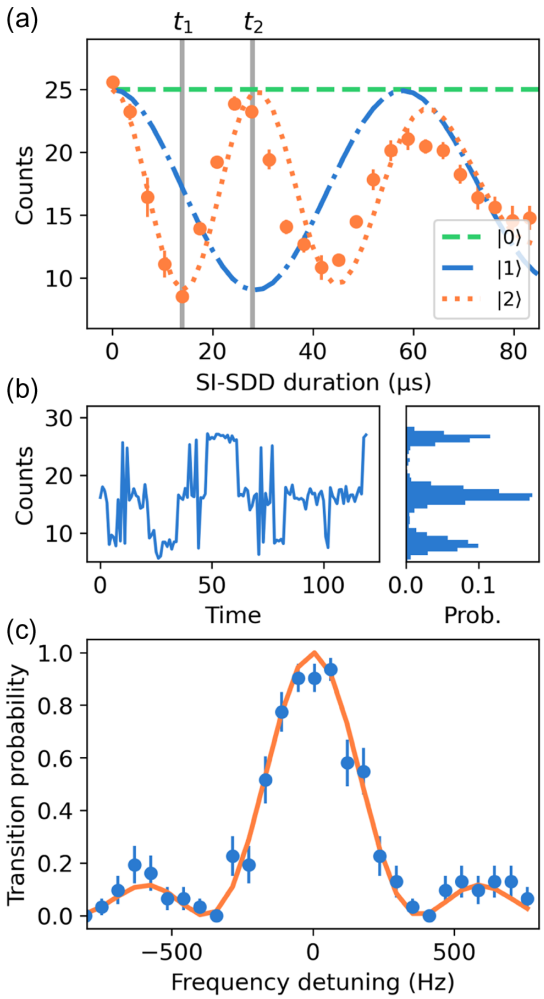

FIG. 4. (a) $^{25}Mg^+$ fluorescence when scanning the duration of the SI-SDD pulse. The observed fluorescence for $N_S = 2$ is plotted along with the expected signal for $N_S = 1$ and 0. All lines come from numerical simulations using measured experimental parameters. (b) Three-level quantum jumps using two $^{25}Mg^+$ and two $^{27}Al^+$ ions. Each data point is an average of 100 measurements. (c) Quantum logic spectroscopy of the $^1S_0 \leftrightarrow {}^3P_0$ transition of two $^{27}Al^+$ SIs. All experiments in this figure are done after 1.25 ms sideband cooling. Error bars represent one standard deviation of the mean.

Choosing the SI-SDD duration to be $t_1 = 14$ μs results in an interferometer phase of $\theta = \pi/2$ for the case $N_{S,\downarrow} = 2$, corresponding to both logic ions flipping from bright to dark. However, for $N_{S,\downarrow} = 1$ there is a 50% transition probability for both LIs, and for $N_{S,\downarrow} = 0$ both LIs remain bright. In Fig. 4(b), we prepare these states probabilistically by scanning the frequency of the 267.4 nm laser over the resonance frequency of the $|\downarrow\rangle_S \rightarrow |c\rangle_S$ transition. The final determination of the number state uses the same adaptive Bayesian process described earlier, yielding the spectroscopy of the $^1S_0 \rightarrow {}^3P_0$ transition as shown in Fig. 4(c). We calculate projection noise limits as a function of both N_L and N_S in the Supplemental Material [26].

Ideally, technical noise σ_{N_S} in determination of $N_{S,\downarrow}$ is negligible compared to the fundamental quantum projection noise limit.

The choice of α and β allow the efficiency of the detection sequence to be optimized and adapted to different measurement bases. For example, if we choose $\alpha\beta = N_S\pi/2$ [$t = t_2$ in Fig. 4(a)], even-parity SI states will result in all LIs bright, whereas odd-parity SI states will result in all LIs dark. This provides an efficient means for performing QLS at the Heisenberg limit [30].

In summary, we have demonstrated a method of performing QLS based on the Schrödinger cat interferometer that allows for scaling both the number of spectroscopy ions and logic ions. This technique operates with ions in thermal motion and is insensitive to the position of the ions in the array. Technical improvements to the current experiment including higher laser power to address all ions equally and improved background gas pressure will allow this protocol to be scaled to longer ion chains. As shown in the Supplemental Material [26], the projection noise in a single detection cycle using this protocol depends on the number of logic ions in addition to the number of spectroscopy ions. In the future, this technique could allow quantum logic spectroscopy in even larger ion ensembles, where some of the same capabilities used here have already been demonstrated [31,32].

We thank D. Barberena for useful discussion and J. J. Bollinger, A. M. Rey, and K. Beloy for their careful reading and feedback on this manuscript. This work was supported by the National Institute of Standards and Technology, the National Science Foundation Q-SEnSE Quantum Leap Challenge Institute (Grant No. 2016244), and the Office of Naval Research (Grant No. N00014-18-1-2634). K. C. was supported by a DOE Office of Science HEP QuantISED award.

*cuikaifeng@apm.ac.cn
†david.hume@nist.gov

[1] J. C. Bergquist, R. G. Hulet, W. M. Itano, and D. J. Wineland, Phys. Rev. Lett. **57**, 1699 (1986).
[2] F. Wolf, Y. Wan, J. C. Heip, F. Gebert, C. Shi, and P. O. Schmidt, Nature (London) **530**, 457 (2016).
[3] C. W. Chou, A. L. Collopy, C. Kurz, Y. Lin, M. E. Harding, P. N. Plessow, T. Fortier, S. Diddams, D. Leibfried, and D. R. Leibrandt, Science **367**, 1458 (2020).
[4] P. Micke, T. Leopold, S. A. King, E. Benkler, L. J. Spieß, L. Schmöger, M. Schwarz, J. R. Crespo López-Urrutia, and P. O. Schmidt, Nature (London) **578**, 60 (2020).
[5] J. M. Cornejo, R. Lehnert, M. Niemann, J. Mielke, T. Meiners, A. Bautista-Salvador, M. Schulte, D. Nitzschke, M. J. Borchert, K. Hammerer, S. Ulmer, and C. Ospelkaus, New J. Phys. **23**, 073045 (2021).
[6] M. S. Safronova, D. Budker, D. DeMille, Derek F. Jackson Kimball, A. Derevianko, and C. W. Clark, Rev. Mod. Phys. **90**, 025008 (2018).
[7] P. O. Schmidt, T. Rosenband, C. Langer, W. M. Itano, J. C. Bergquist, and D. J. Wineland, Science **309**, 749 (2005).
[8] D. B. Hume, T. Rosenband, and D. J. Wineland, Phys. Rev. Lett. **99**, 120502 (2007).
[9] K. Beloy *et al.* (Boulder Atomic Clock Optical Network (BACON) Collaboration), Nature (London) **591**, 564 (2021).
[10] S. Hannig, L. Pelzer, N. Scharnhorst, J. Kramer, M. Stepanova, Z. T. Xu, N. Spethmann, I. D. Leroux, T. E. Mehlstäubler, and P. O. Schmidt, Rev. Sci. Instrum. **90**, 053204 (2019).
[11] K. Cui, S. Chao, C. Sun, S. Wang, P. Zhang, Y. Wei, J. Yuan, J. Cao, H. Shu, and X. Huang, Eur. Phys. J. D **76**, 140 (2022).
[12] S. M. Brewer, J.-S. Chen, A. M. Hankin, E. R. Clements, C. W. Chou, D. J. Wineland, D. B. Hume, and D. R. Leibrandt, Phys. Rev. Lett. **123**, 033201 (2019).
[13] C. W. Chou, D. B. Hume, M. J. Thorpe, D. J. Wineland, and T. Rosenband, Phys. Rev. Lett. **106**, 160801 (2011).
[14] D. B. Hume, C. W. Chou, D. R. Leibrandt, M. J. Thorpe, D. J. Wineland, and T. Rosenband, Phys. Rev. Lett. **107**, 243902 (2011).
[15] T. R. Tan, J. P. Gaebler, Y. Lin, Y. Wan, R. Bowler, D. Leibfried, and D. J. Wineland, Nature (London) **528**, 380 (2015).
[16] D. Kienzler, Y. Wan, S. D. Erickson, J. J. Wu, A. C. Wilson, D. J. Wineland, and D. Leibfried, Phys. Rev. X **10**, 021012 (2020).
[17] M. Schulte, N. Lörch, I. D. Leroux, P. O. Schmidt, and K. Hammerer, Phys. Rev. Lett. **116**, 013002 (2016).
[18] J.-S. Chen, K. Wright, N. C. Pisenti, D. Murphy, K. M. Beck, K. Landsman, J. M. Amini, and Y. Nam, Phys. Rev. A **102**, 043110 (2020).
[19] L. Feng, W. L. Tan, A. De, A. Menon, A. Chu, G. Pagano, and C. Monroe, Phys. Rev. Lett. **125**, 053001 (2020).
[20] C. Monroe, D. M. Meekhof, B. E. King, and D. J. Wineland, Science **272**, 1131 (1996).
[21] A. R. Milne, C. Hempel, L. Li, C. L. Edmunds, H. J. Slatyer, H. Ball, M. R. Hush, and M. J. Biercuk, Phys. Rev. Lett. **126**, 250506 (2021).
[22] P. C. Haljan, K.-A. Brickman, L. Deslauriers, P. J. Lee, and C. Monroe, Phys. Rev. Lett. **94**, 153602 (2005).
[23] C. Hempel, B. P. Lanyon, P. Jurcevic, R. Gerritsma, R. Blatt, and C. F. Roos, Nat. Photonics **7**, 630 (2013).
[24] K. Mølmer and A. Sørensen, Phys. Rev. Lett. **82**, 1835 (1999).
[25] D. J. Wineland, C. Monroe, W. M. Itano, D. Leibfried, B. E. King, and D. M. Meekhof, J. Res. Natl. Inst. Stand. Technol. **103**, 259 (1998).
[26] See Supplemental Material at http://link.aps.org/supplemental/10.1103/PhysRevLett.129.193603 for more detailed discussion about the measurement scheme.
[27] J.-S. Chen, S. M. Brewer, C. W. Chou, D. J. Wineland, D. R. Leibrandt, and D. B. Hume, Phys. Rev. Lett. **118**, 053002 (2017).
[28] T. Rosenband, P. O. Schmidt, D. B. Hume, W. M. Itano, T. M. Fortier, J. E. Stalnaker, K. Kim, S. A. Diddams, J. C. J. Koelemeij, J. C. Bergquist, and D. J. Wineland, Phys. Rev. Lett. **98**, 220801 (2007).

[29] S. D. Erickson, J. J. Wu, P.-Y. Hou, D. C. Cole, S. Geller, A. Kwiatkowski, S. Glancy, E. Knill, D. H. Slichter, A. C. Wilson, and D. Leibfried, Phys. Rev. Lett. **128**, 160503 (2022).

[30] J. J. Bollinger, W. M. Itano, D. J. Wineland, and D. J. Heinzen, Phys. Rev. A **54**, R4649 (1996).

[31] K. A. Gilmore, J. G. Bohnet, B. C. Sawyer, J. W. Britton, and J. J. Bollinger, Phys. Rev. Lett. **118**, 263602 (2017).

[32] M. Affolter, K. A. Gilmore, J. E. Jordan, and J. J. Bollinger, Phys. Rev. A **102**, 052609 (2020).